ACS APPLIED MATERIALS & INTERFACES

Research Article

www.acsami.org

Oscillating Friction on Shape-Tunable Wrinkles

Kosuke Suzuki,*[,†] Yuji Hirai,[‡] and Takuya Ohzono*[,†]

[†]Nanosystem Research Institute, National Institute of Advanced Industrial Science and Technology (AIST), 1-1-1 Higashi, Tsukuba 305-8565, Japan

[‡]Chitose Institute of Science and Technology, 758-65 Bibi, Chitose 066-8655, Japan

Supporting Information

ABSTRACT: Friction on soft materials is strongly correlated with the associated deformation, which may be controlled by the surface topography. We investigate the wearless sliding friction between a rigid hemispherical indenter and a deformable textured surface, which is shape-tunable wrinkles. The size of the indenter is comparable to the wavelength of the wrinkles. We evaluate the effects on the friction of the aspect ratio of the wrinkles, the applied normal load, and the alignment direction of the wrinkles relative to the sliding direction. The frictional oscillations are observed during sliding in the direction perpendicular to the alignment using optical images and friction profiles. The correlation of friction force oscillation with deformation of the wrinkles is elucidated using Hertz contact theory. Within a cycle of frictional oscillation, the friction force increases as the front part of the indenter elastically plows the crests. When the normal load is high and/or the aspect ratio of the wrinkles is low, the indenter continues to squash the wrinkles and remains in contact with them during sliding. Consequently, the amplitude of friction force oscillation relative to the averaged friction force decreases.

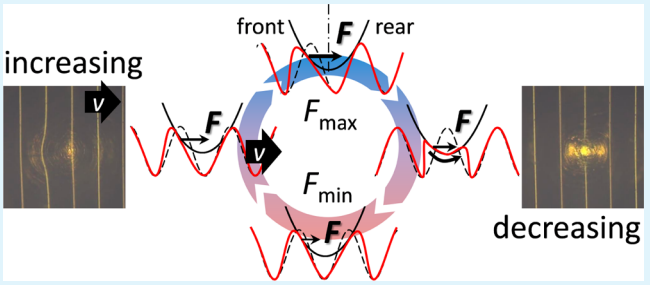

KEYWORDS: *wrinkles, deformable microstructure, textured surface, friction, surface buckling*

INTRODUCTION

Living things such as animals, insects, and plants exhibit a wide variety of soft textured surfaces that make contact with surrounding matter. The asperities of the textured surfaces contribute to their tribological properties, for example, adhesion,[1−6] lubrication,[7] and friction (on a finger pad).[8−10] In particular, the asperities of the soft textured surface deform greatly under sliding friction, and the deformation can be continuous, periodic, or intermittent. The dynamics of the deformation should affect the fluctuations in the friction force and its average. An understanding of the relationship between the deformation and friction provides useful information for engineering the friction at soft interfaces, which is an important process in biomimetics.[1] However, it is difficult to understand directly the mechanism of friction on soft living surfaces because it is associated with the time-dependent deformation of complicated hierarchical structures. Therefore, as a first step, it is important to study the friction using a simplified surface structure, which makes analysis easier.

In addition to the actively studied friction between hard asperities and soft flat surfaces,[11−17] the effects of various artificial "soft asperities" on frictional phenomena, e.g., contact, deformation, adhesion, and friction, have also been investigated.[18−35] Soft textured rubbers can deform locally, and the total area and number of the contacts depend nonlinearly on the applied normal load,[20,21,24−26] which is the main difference from a surface without asperity. To understand contact problems correctly, some theoretical approaches[18,19,22,23,35] based on, e.g., the Johnson−Kendall−Roberts framework,[19] are necessary. Regarding friction on a soft textured surface, Rand and Crosby reported interesting results when they used aligned wrinkles[36−39] imprinted on an elastomer [poly(dimethylsiloxane) = PDMS] surface.[29] They reported that the averaged friction force was reduced and that the oscillation of the friction force generated on a smooth PDMS surface by the formation of Schallamach waves[40,41] was suppressed on the wrinkled surface. In their experiments, the radius of the hemispherical indenter was roughly 100 times larger than the wavelength of the wrinkles, λ. Therefore, the friction that occurs when the radius of the indenter is comparable to λ remains to be studied, and the result will illuminate how the spatiotemporal deformation of soft textures contributes to the friction.

To conduct such an experiment, we can use shape-tunable wrinkles;[42] the depth and direction of the wrinkle grooves can be reversibly controlled by applying a strain.[24,36−39,43−46] This property has been applied to shape liquids at small scales by controlling capillary phenomena through changes in the microgroove shape[24,39,46,47] to control the liquid-crystal alignment[47] and to control the optical properties.[42] With the

Received: February 20, 2014
Accepted: April 11, 2014
Published: April 11, 2014

shape-tunable wrinkles, the shape-dependent frictional forces are expected to be controlled simply by the applied strain, and the tunability of the friction may be applicable to, e.g., touch-screen devices.[48,49]

In this article, we investigate the wearless sliding friction and frictional oscillation on shape-tunable wrinkles in contact with a rigid hemispherical indenter. In particular, we focus on the positional relationships between the wrinkles and sliding indenter, which is supported by one or a few wrinkle crests. We evaluate the frictional oscillations with respect to the shape of the wrinkles (the aspect ratio), the applied normal load, and the alignment direction of the wrinkles relative to the sliding direction. We discuss the cycle of deformation in wrinkles during sliding and the corresponding friction force on the basis of experimental observations and Hertz contact theory.

EXPERIMENTAL SECTION

Sample Preparation. Shape-tunable wrinkles were prepared by attaching a thin polyimide (PI) film (Nilaco, Kapton; thickness of 12.5 μm and elastic modulus of 2.5 GPa) onto an elastomeric PDMS substrate as follows.[42] The PDMS elastomer (Dow Corning, Sylgard 184; 10:1 mixing ratio of base to curing agent) was cured on a smooth glass plate. The smooth surface of the PDMS substrate (25 × 25 × 5 mm^3) was weakly treated using argon plasma (SEDE-P, Meiwa Forsis) to enhance the wetting of isopropyl alcohol (Sigma-Aldrich). An isopropyl alcohol solution (5 wt %) of an elastic adhesive (Cemedine, Super-X2) was coated on the activated PDMS surface using a spin coater (MSA-150, Mikasa) at 2000 rpm for 20 s; soon after this, the PI film was placed on the surface. The sample was pressed (~2 kPa) between two flat glass plates for tight adhesion for at least 12 h at 25 °C. To induce wrinkles, a uniaxial compressive strain (s: 0−7.5%) was applied to a sample using a homemade vise. The shapes of the wrinkles were measured by a laser microscope (VK9710, Keyence).[42]

Experimental Setup. The friction force was measured by a pin-on-plate friction tester (IMC-9006, Imoto Machinery) equipped with an inverted reflection microscope (GX41, Olympus). The experimental setup is shown in Figure 1. For the friction force measurements, we used an indenter with a hemispherical shape (R = 1.0 mm, SUS 304 stainless steel), which was connected to a beam-type load cell (WBJ-05N, Showa Measuring Instruments). The sample held by a vise was mounted on a linear sliding stage for frictional sliding. The alignment of the wrinkles was set either parallel or perpendicular to the sliding direction. Microscopic images of the frictional interface and surrounding area were continuously recorded using a video camera (HDR-CX430 V, Sony, 30 frames/s). A time series of the recoded images was reconstructed into a spatiotemporal image to investigate the temporal evolution of deformation of the wrinkled surface.

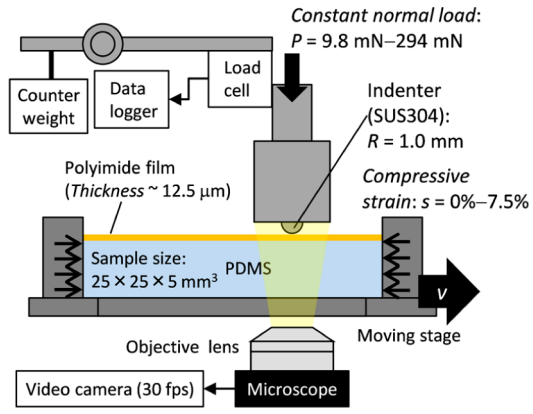

Figure 1. Schematic illustration of our experimental setup for friction measurement and in situ observation.

The experiments were conducted in air at a temperature of 26.5 ± 0.5 °C and a relative humidity of 60 ± 10%. The indenter and sample surface were wiped using a cotton cloth wetted by acetone before each friction measurement. Sliding of the sample was begun 15 s after the moment of contact between the indenter and sample surface. The applied normal load during sliding was held constant in the range from 9.8 to 294.0 mN. The sliding speed of the linear stage was fixed at either 0.1 or 0.3 mm/s. This slow speed range was chosen because the actual normal load was well regulated with the balance-type instrument (Figure 1) and clearer optical observation was possible. The lower detection limit of the friction force was 0.1 mN. The averaged friction force was calculated from the raw friction forces during sliding for a total of 54 mm, omitting the data for the initial 5 mm of sliding, for a specific set of sliding conditions, e.g., applied strain s and normal load.

RESULTS AND DISCUSSION

Shape Tunability of a Wrinkled Surface. When the applied strain exceeded 1.4%, the sample surface buckled into wrinkles. The spatial wavelength of the wrinkles, λ, decreased slightly as the strain increased further. In addition, the amplitude h exhibited an inverse-quadratic increase from 43 to 103 μm (Figure 2a). Because the strain dependence of λ was small, the aspect ratio (h/λ) also showed inverse-quadratic increase with respect to s and changed from 0.073 to 0.185 (Figure 2b). Parts c and d of Figure 2 show reflection microscopic images of the sample surfaces. The flat surface (at s = 0%) showed no pattern (Figure 2c). In contrast, the wrinkled surface (at s = 7.5%) showed periodic bright lines, each of which corresponds alternately to either the bottom or top of the wrinkled surface (Figure 2d). When the center of the indenter was in contact with the sample surface, a bright spot formed at the contact area [e.g., Figure 3b(i−viii)]. Moreover, multiple reflections from the surfaces of both the indenter and sample around the contact area formed slightly bright regions [around the bright spot, e.g., Figure 3b(i−viii)]. This effect was remarkable when the center of the indenter was not in contact with the wrinkled surface [e.g., Figure 3b(ix), as indicated by a white arrow]. The reason for this would be the complicated reflection at the air gap with curved interfaces under the indenter.

Typical Friction Profiles and Indenter-Induced Deformation of Wrinkles. Figure 3 shows typical friction profiles and microscopic images observed during sliding at a constant sliding speed of 0.3 mm/s at various normal loads and strains on wrinkles that were aligned perpendicular to the sliding direction (see also the movie file in the Supporting Information, SI). The friction force oscillated on the wrinkled surfaces with a periodicity identical with that of the wrinkles independent of the normal loads and aspect ratio of the wrinkles. In addition, the friction force was higher at a higher normal load, and the amplitude of the oscillation was larger at a higher normal load and/or larger strain (Figure 3a). The periodic oscillation of the friction force was not observed on the flat surfaces (s = 0%); this was also the result when the wrinkles were aligned parallel to the sliding direction (Figure S1 in the SI). This also suggests that no observable Schallamach wave developed in our system.[29,40,41] In situ microscopic images taken during sliding between the surface and indenter show that deformation of the wrinkles in contact with the indenter depends on the applied normal loads and strain (Figure 3b). A larger deformation area was observed under a higher normal load. Under lower loads, one or two crests were deformed [Figure 3b(v, vi, viii, ix)], and

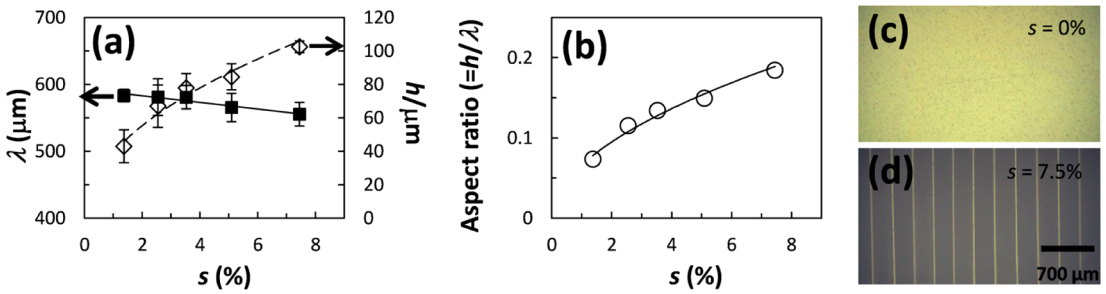

Figure 2. Characteristic lengths of shape-tunable wrinkles and optical images. (a) Plots of wavelength λ (◇) and amplitude h (■) with respect to applied strain s. (b) Plot of aspect ratio h/λ with respect to s. Microscopic images of (c) flat and (d) wrinkled surfaces.

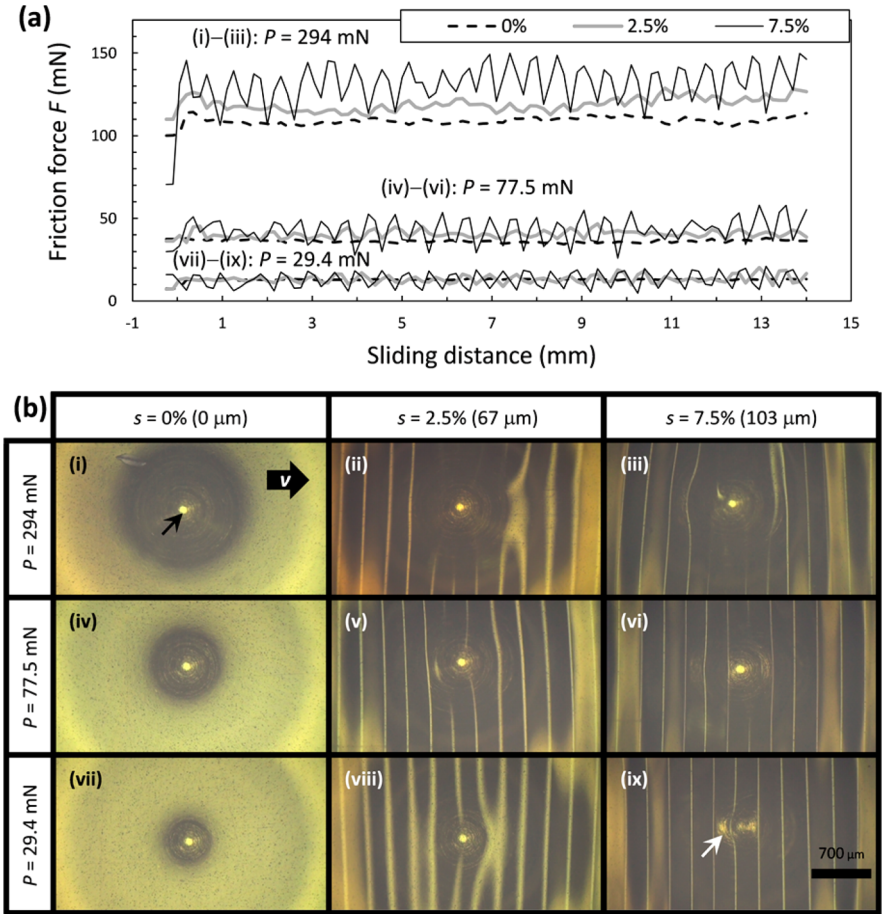

Figure 3. Typical friction profiles and snapshots of wrinkled and flat surfaces under friction. (a) Friction profiles of wrinkles aligned perpendicular to the sliding direction [gray bold lines, s = 2.5% (h = 67 μm); solid lines, (s = 7.5% and h = 103 μm)] and flat surfaces (broken lines). (b) In situ observation of the friction surface under optical microscopic images. The applied normal loads are P = 294 mN for i–iii, 77.5 mN for iv–vi, and 29.4 mN for vii–ix. The bold black arrow indicates the direction of sliding of the sample surface with speed v = 0.3 mm/s. The black arrow in b(i) indicates the center of the indenter, which remains in the images. The white arrow in b(ix) indicates a bright area originating from enhanced multiple reflections when the center of the indenter is not in contact with the wrinkled surface.

two or more crests were deformed under higher loads [Figure 3b(ii, iii)]. As discussed later, the normal-load-dependent different modes of contact affect the oscillation of the friction. Note that the wrinkles showed neither delamination of the surface film nor clear scarring even under the highest normal load used (P = 294 mN). In the following sections, we describe the averaged friction forces and the details of the friction profiles, which are based on the typical raw data shown in Figure 3a.

Averaged Friction Forces. The averaged friction force F_{av} depends almost linearly on the normal load (Figure 4a). The plots include results from the previously described different frictional states in terms of the modes of contact, which depend on both the normal load and aspect ratio of the wrinkled surfaces. Thus, this linearity should be a result from a complicated interplay between the effects of the contact states and deformation of the wrinkles. Moreover, also the effect of the PI film might be involved in this scenario because the plots for the flat PI-capped PDMS also show almost a linear relationship instead of the power law one,[50,51] which is widely observed for the friction on the soft substrate (without the capping film). Nevertheless, from the results, we can discuss the

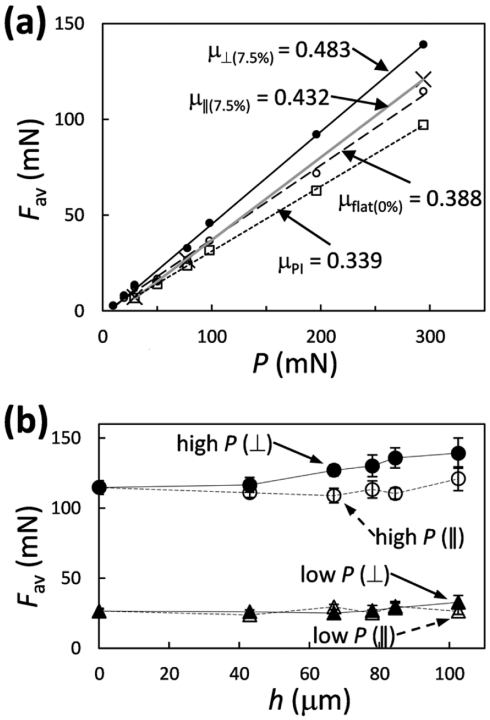

Figure 4. Averaged friction forces (F_{av}) on wrinkled surfaces. (a) F_{av} versus P. Symbols: (○) flat surface (s = 0%); (●) wrinkles (s = 7.5%, h = 103 μm) aligned perpendicular to the sliding direction (⊥); (×) wrinkles aligned parallel to the sliding direction (∥); (□) PI film on a glass plate. (b) F_{av} versus A (amplitude of wrinkles) obtained under different sliding directions (closed symbols, ⊥; open ones, ∥) and different normal loads (triangles, P = 77.5 mN; circles, P = 294 mN).

trend of the friction that depends on the surface states (flat or wrinkled) and sliding direction as follows.

The coefficient of friction (COF) on a PI film attached to a PDMS surface was larger than that on an identical PI film on a glass plate. The difference is likely due to the difference in Young's moduli of the underlayers, which affect frictional dissipation. A similar effect originating from deformation of the underlayer was reported for rubber samples with different thicknesses.[52] When the surface was wrinkled, especially when the wrinkles were aligned perpendicular to the sliding direction, the COFs were slightly larger than those on the flat surface. This result seemingly contradicts the apparent reduction in the friction on wrinkles reported by Rand and Crosby.[29] However, considering that, in our system, no Schallamach wave was observed even on the flat surface, it is reasonable to lose the reduction effect. Thus, it is also generally suggested that the effect of the soft asperities on the friction depends on whether Schallamach waves develop on a flat surface of the same material. [Here, we can consider two reasons for suppressing the Schallamach wave on the present flat (unwrinkled) PI film supported by soft PDMS as follows. (1) The surface-chemistry-dependent interfacial adhesive strength is smaller for the PI surface; PI is less sticky than PDMS. (2) The Schallamach wave can be considered as a shear-stress-induced buckling of the surface. Therefore, the hard PI film can suppress the buckling of the surface compared to the case without the capping film.]

Figure 4b shows the effect of the applied strain, which controlled the amplitude of the wrinkles, on the averaged friction force. The data on the wrinkled surfaces aligned perpendicular or parallel to the sliding direction under two different applied normal loads are shown. When the applied normal load was small (77.5 mN), the averaged friction forces were almost constant, and the difference between the two alignment directions was small. When the applied normal load was high (~294 mN), the difference became larger. That is, the averaged friction force on the perpendicularly aligned wrinkles clearly increased with the strain, but that on the surface aligned parallel changed little. Note that various contact situations can be considered when the indenter slides in parallel with the wrinkle grooves; the indenter is, e.g., in contact with the top of the crest, with the bottom of the groove, and between them. The data shown in Figure 4b as open symbols are averaged values over the various contact situations.

Next, we qualitatively discuss the origin of the observed difference in the average friction forces shown in Figure 4. The present frictional system involves three generic mechanisms: (i) adhesion models at adjacent interfaces; (ii) plowing models; (iii) the Coulombic interlocking mechanism.[51] In the adhesion model, the energy dissipation process resulting from the shear of adhesive junctions in regions immediately adjacent to the interface is considered, which is a simple system of friction with small deformation on a flat surface. In the plowing model, the large deformation and plowing of the soft substrate and the viscoelastic energy dissipation are considered. In the Coulombic interlocking mechanism, the geometric effect of the slope of the nonflat and relatively rigid surface is considered. Because the averaged friction force is enhanced on the wrinkled surface, the Coulombic interlocking mechanism is most likely applied. However, as we discuss later, the wrinkles are largely deformed/plowed even under the lower normal load. Thus, it is difficult to conclude that the origin of the enhancement is purely the Coulombic interlocking mechanism. Rather the enhancement resulted from the nonadditive interplay between the three mechanisms above, which remains to be studied with a more detailed theoretical model.

Nevertheless, the effect of wrinkled topography on the total friction force can be discussed in terms of the above three mechanisms and roughly quantified using the experimental data shown in Figure 4a as follows. (A) The friction on the PI film attached to a rigid glass slide corresponds to the contribution of the adhesion model. (B) The friction on the PI film attached to the soft substrate (PDMS) includes the adhesion and plowing models. Thus, the friction enhanced from case A to case B, which is the actual effect of the soft substrate on the averaged friction force, can be attributed to the contribution of deformation/plowing of the substrate. (C) Finally, the friction on the wrinkled PI film includes the adhesion and plowing models and the Coulombic interlocking mechanism. Thus, the Coulombic interlocking mechanism mixed with deformation/plowing of the asperity of wrinkle topography can account for the friction enhanced from case B to case C, which is the actual effect of the wrinkles on the averaged friction force. On the average over the present range of the normal load, this contribution accounts for ~20% of the total friction estimated from the COFs shown in Figure 4a; we can tune ~20% of the total friction purely by changing the wrinkle topography. Similarly, the contribution of the adhesion model at an adjacent interface accounts for ~60%, and the sum of those of the two other mechanisms, the Coulombic interlocking and plowing, accounts for ~40% of the total friction on the wrinkled surface.

The present results indicate that the friction force can be controlled by changing the shape and/or alignment direction of

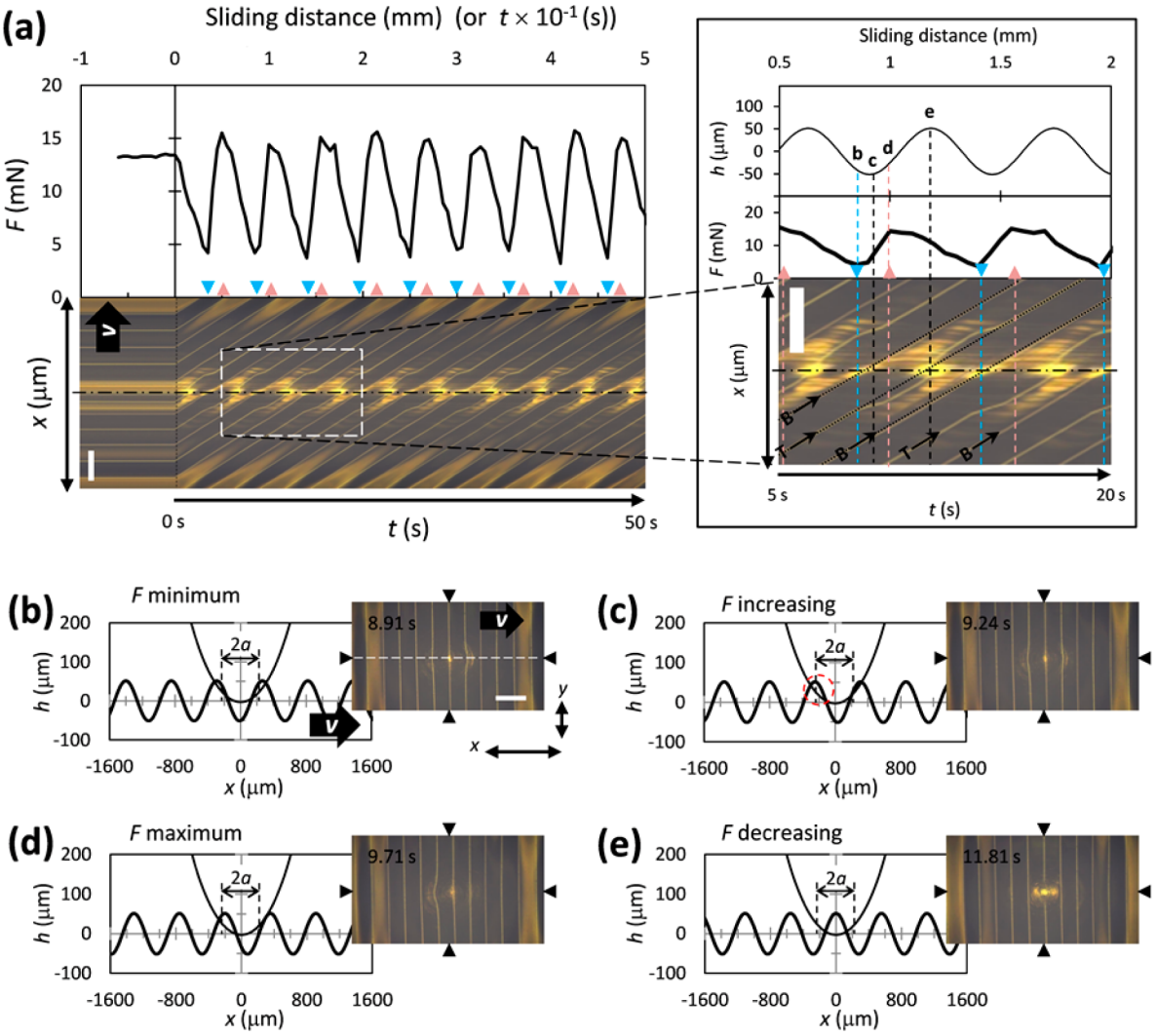

Figure 5. Oscillation of the friction force on a wrinkled surface under low normal load (P = 29.4 mN) and schematics of the positional relationship between the surface and indenter. (a) Friction profile on a wrinkled surface (s = 7.5% and h = 103 μm) and spatiotemporal pattern along the white broken line in part b over 50 s. (Inset) Magnified image of the spatiotemporal pattern from 5 to 20 s and corresponding friction force and undeformed surface profiles. Black dotted diagonal lines correspond to the original bottom (B) and top (T) positions. Schematics of states when F is (b) minimum (indicated by the broken blue lines in the inset), (c) increasing, (d) maximum (indicated by the broken pink lines in the inset), and (e) decreasing. The bold arrows indicate the sliding direction of the sample with speed v = 0.1 mm/s (scale bars: 500 μm).

the wrinkles. More importantly, the present shape-tunable wrinkles enable us to change both of them reversibly and repeatedly on one sample by changing the degree and/or anisotropy of the applied strain.[42] The mechanism of the present geometry-dependent friction, which includes the different frictional states caused by the applied strain and alignment direction, must be correlated with the contact state between the deformable wrinkled surface and indenter. To investigate the correlation, we focus on the details of the friction profile and corresponding images of the surface deformation in the next section; the results at a sliding speed of 0.1 mm/s, which do not differ greatly from those at 0.3 mm/s, will be analyzed in detail.

Friction Profiles and Spatiotemporal Patterns on Wrinkled Surfaces. To clarify the contact states during frictional oscillation on perpendicularly aligned wrinkled surfaces (e.g., Figure 3a), we tracked the time evolution of the positional relationship between wrinkled surfaces and an indenter and of the deformation around the contact region. Figure 5a (upper) shows the friction profile under a low load (29.4 mN), which exhibits a periodic oscillation similar to that shown in Figure 3a. The decreasing period in the oscillation was longer than the increasing one; the profile shows an antisawtooth shape, which is a time-reversed shape generally observed and estimated for stick–slip motions.[53−56] Figure 5a (lower) shows the corresponding spatiotemporal pattern. The diagonal bright lines correspond to crests or grooves on the wrinkled surface, and the slopes are equal to the sliding speed v. As shown in the optical images in Figure 5b–e, the bright lines under the indenter deviate from the straight lines, indicating deformation of the crests of the wrinkles. At a position away from the contact area, the wrinkled surface retained its original shape. This phenomenon appears in the spatiotemporal pattern as a deviation of the bright lines from the diagonal straight lines, which is clearly noted in their deviation from the dotted lines shown in Figure 5a (inset). The lines with large deviations were assigned to the crests of the wrinkles. The bright lines assigned to the grooves were straight, suggesting that the bottom of the grooves was not in contact with the indenter; i.e., the grooves were not deformed at the bottom. In addition, the friction

dx.doi.org/10.1021/am5010738 | ACS Appl. Mater. Interfaces 2014, 6, 10121−10131

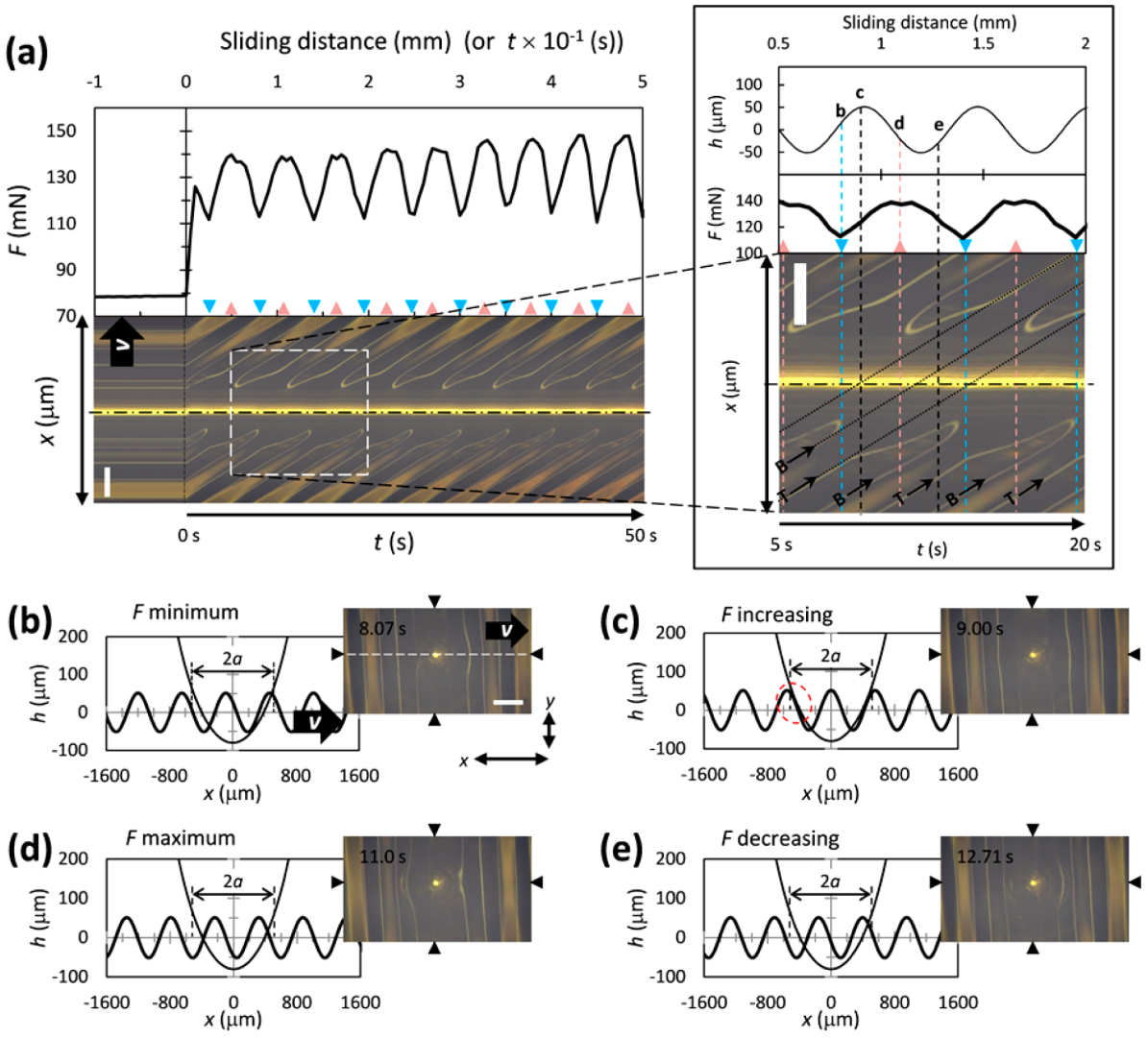

Figure 6. Oscillation of the friction force on the wrinkled surface under high normal load (P = 294 mN) and schematics of the positional relationship between the surface and indenter. (a) Friction profile on a wrinkled surface (s = 7.5% and h = 103 μm) and spatiotemporal pattern along the white broken line in part b over 50 s. (Inset) Magnified image of the spatiotemporal pattern from 5 to 20 s and corresponding friction force and undeformed surface profiles. Black dotted diagonal lines correspond to the original bottom (B) and top (T) positions. Schematics of states when F is (b) minimum (indicated by the broken blue lines in the inset), (c) increasing, (d) maximum (indicated by the broken pink lines in the inset), and (e) decreasing. The bold arrows indicate the sliding direction of the sample with speed v = 0.1 mm/s (scale bars: 500 μm).

profile differs from the topographic profile of the wrinkles [Figure 5a (inset)]; the broken blue and pink lines with arrowheads correspond to the states showing the minimum and maximum of the friction force, respectively.

A cycle of oscillation of the friction force is summarized as follows, focusing on the positional relationships between the wrinkles and indenter and on deformation of the wrinkles:

(a) The friction force is minimum when the center of the indenter is located between two crests, with which the front and rear parts of the indenter are in contact. Both crests undergo comparable deformation [Figure 5a (inset), on blue broken lines].

(b) The friction force increases when deformation of the crest in contact with the front part of the indenter increases, during which the indenter transiently plows the crest (the phenomenon is called "elastic plowing"[1,57] here). Thus, both increasing effects of the Coulombic interlocking and plowing of the wrinkled surface at this period account for increasing friction force. At the same time, deformation of the crest in contact with the rear part of the indenter decreases (Figure 5c, blue to pink broken lines).

(c) The friction force is a maximum when deformation of the crest in contact with the front part of the indenter is considered to be the largest and deformation of the crest in contact with the rear part of the indenter has disappeared (Figure 5d, on pink broken lines).

(d) The friction force decreases when the crest passes the center of the indenter in contact. During this period, only the crest is in contact with the indenter (single contact). After the pass, the crest starts to recover its original shape (Figure 5e, pink to blue broken lines).

Each of these four states is schematically shown in Figure 5b–e with its corresponding microscopic image. The positional relationships between the wrinkles and indenter along the x axis are shown in the schematic side-view images. Note that deformation of the wrinkles is not expressed in the schematics. The surface profile in the schematic was reproduced using a cosine function, $f(x) = (h/2)\cos(2\pi x/\lambda)$, where h and λ are the

dx.doi.org/10.1021/am5010738 | ACS Appl. Mater. Interfaces 2014, 6, 10121–10131

amplitude and wavelength, respectively, and the experimentally observed values at s = 7.5% (Figure 2a) were used for them. The hemispherical indenter with a radius of 1 mm appears as a quadratic curve, and the amplitude is enlarged because a larger magnification was used in the z direction for visibility. To predict the possible contacts, these curves were superimposed because deformation of the wrinkle and the position of the indenter in the z direction were not considered in the schematics. When the apparent contact diameter ($2a \sim 471$ μm, indicated in the figures) roughly estimated on the basis of the Hertz contact problem (discussed later) was introduced, two representative contact states were predicted, as follows. In one state, the indenter was supported by two deformed crests, i.e., a partial contact (Figure 5b–**d**). In the other state, the indenter was supported by one crest, i.e., a single contact (Figure 5e). These two states were consistent with the deformation observed in the microscopic images.

Next, Figure 6a shows the friction profile and spatiotemporal pattern under a high normal load (294 mN), which exhibits a typical frictional state with larger deformation on the wrinkle than that under a low load. Oscillation of the friction force [Figure 6a (upper)] exhibits a roughly triangular waveform, in which the decreasing periods are shorter than those under the low load (Figure 5a). The brightest straight line in the spatiotemporal pattern indicates that the center of the indenter remains in contact with the wrinkled surface during sliding [Figure 6a (lower)]. Neighboring bright lines in the spatiotemporal pattern, which correspond to the horizontal parts of the surface, such as the bottom of the groove and top of the crest, are connected near the center of the indenter. The bright line assigned to the top of the crest starts to deviate from the original position (dotted line in the inset of Figure 6a), indicating that the top of the crest was shifted toward the direction opposite to the sample sliding direction. This shift was caused by transient deformation of the crest due to the elastic plowing phenomenon. After the shifted top of the crest reached the position of the groove bottom, they coalesced and annihilated each other, indicating that the horizontal parts disappeared; this corresponds to the turn in the bright line in the spatiotemporal pattern. Again, when we introduce the apparent contact diameter under the high load ($2a \sim 1015$ μm $> \lambda$, as indicated in the figures) roughly estimated on the basis of the Hertz contact problem, we find that two or three crests could support the indenter (Figure 6b–e). The friction force increases when deformation of the crest in contact with the frontmost part of the indenter, indicated by the red broken circle in Figure 6c, increases. This positional relationship was also maintained under the low load, as described previously. The sample surface at the rear of the indenter recovered its original wrinkled shape even though the surface had been strongly deformed (squashed) directly beneath the center of the indenter.

On a wrinkled surface with a low aspect ratio of 0.12 (h = 67 μm, λ = 581 μm, and s = 3.5%) under a low normal load (29.4 mN), the brightest straight line in the spatiotemporal pattern indicates that the center of the indenter remains in contact with the wrinkled surface during sliding (Figure 7). This result is qualitatively similar to that in Figure 6. The low aspect ratio of the surface reduced the applied load required to maintain continuous contact between the wrinkled surface and center of the indenter.

Standard Deviation of the Oscillating Friction Force Relative to the Averaged Friction Force. The averaged

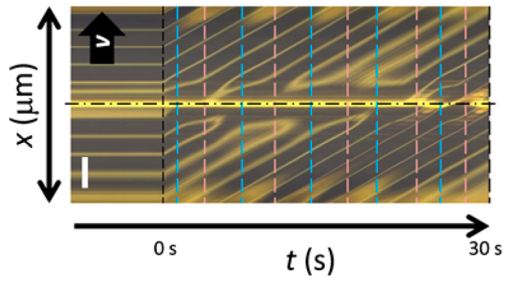

Figure 7. Spatiotemporal pattern obtained with low-aspect-ratio wrinkles (s = 3.5% and h = 78 μm) at low normal load (P = 29.4 mN). Scale bar: 500 μm.

friction forces increased with the applied load independently of the aspect ratio (Figure 4a). The corresponding amplitude of the oscillating friction force was roughly constant for low-aspect-ratio wrinkles (s = 2.5% and h = 67 μm) and increased for high-aspect-ratio wrinkles (s = 7.5% and h = 103 μm; Figure 3a) when the applied load increased. Here, we introduce the standard deviation of the oscillating friction force, σ_F, which directly relates to the amplitude. The magnitude of σ_F reflects the mixed effects of the Coulombic interlocking and the periodic deformation/plowing of the wrinkled shape (and not the stationary friction, which are the averaged shear deformation of the substrate and the averaged interfacial adhesion). In simple words, σ_F reflects the effect of the deformable wrinkled topography. Therefore, it tends to increase with the aspect ratio of the wrinkles and the normal load, as read from Figure 3a. To evaluate the relative effect of the above-mentioned deformable wrinkled topography on that of the stationary friction, here we introduce the values of σ_F/F_{av} (Figure 8). σ_F/F_{av} decreased steeply with the load when the

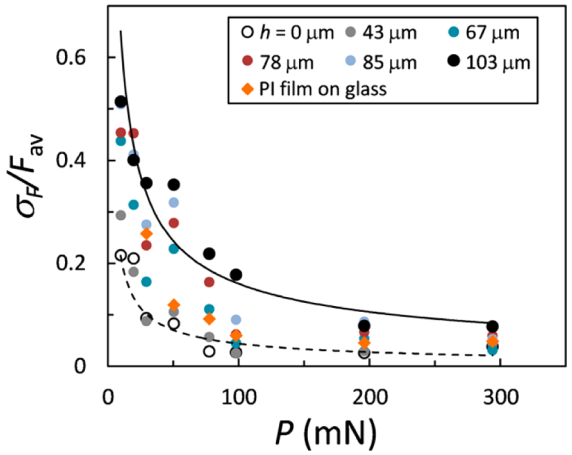

Figure 8. Plots of σ_F/F_{av} versus P at various h. Curves are guides for the eyes (solid line, h = 103 μm; dotted line, h = 0 μm).

normal load was below 100 mN and became almost constant under higher loads. The original shape of the wrinkles was strongly reflected in the friction profile under low loads because deformation of the wrinkles was relatively small (Figure 5). In contrast, the original shape was weakly reflected in the friction profile under high loads because the wrinkles were strongly deformed and lost their periodicity under the indenter (Figure 6). The trend of these results was remarkable at s = 7.5% (wrinkles with a high aspect ratio, h = 103 μm) because the deformable volume was the largest. The data in the region of

dx.doi.org/10.1021/am5010738 | ACS Appl. Mater. Interfaces 2014, 6, 10121–10131

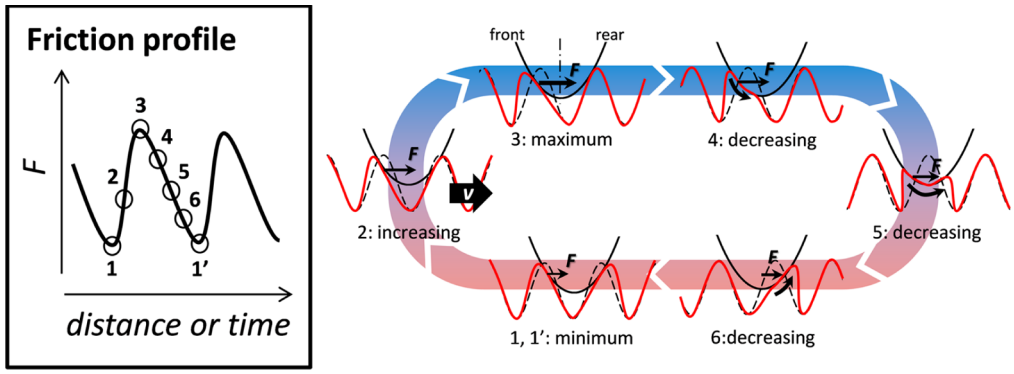

Figure 9. Schematic illustration of the friction profile and corresponding cycle of surface deformation observed on wrinkles with a high aspect ratio under a low load.

lower σ_F/F_{av} correspond to the state in which the deformed surface was in continuous contact with the center of the indenter (Figures 6 and 7). This result suggests that, on the shape-tunable wrinkles, the amplitude of the frictional oscillation can be tuned to a certain degree with a change in the applied strain (the aspect ratio) and/or the normal load.

Rough Estimate of the Contact States by Hertz Contact Theory. Assuming that the effect of adhesion is negligible, the present results should probably be understood in the regime of Hertz contact theory[58,59] (and the extended version[60]). However, to discuss the contact states crudely in terms of the characteristic length of the contact, we avoid treatment of the space-time-dependent and complicated deformation of the wrinkled surface directly; thus, the surface is assumed to be flat. Although this assumption is too coarse to give quantitative values, a rough estimate of the characteristic contact radius and penetration depth can be obtained as a first approximation. This assumption is also supported by the low aspect ratio of the wrinkled surface (0.2 at most). Consequently, the problem is treated as that of contact between an elastic half-space and a rigid hemisphere. The contact radius a and penetration depth d are given by

$$a = (3PR/4E^*)^{1/3} \quad (1)$$

$$d = (3P/4E^*)^{2/3}/R^{1/3} \quad (2)$$

where P, R, and E^* are the normal load, radius of the hemisphere, and relative Young's modulus, respectively. E^* is derived from the equation $1/E^* = (1 - \nu_i^2)/E_i + (1 - \nu_{hs}^2)/E_{hs}$, where E_i, E_{hs}, ν_i, and ν_{ha} are Young's moduli of the indenter and half-space and Poisson's ratios of the indenter and half-space, respectively. The second term is negligible because E_i (~200 GPa) $\gg E_{ha}$ (1.3 MPa). Here, the Young's modulus of the PI film is much larger than that of PDMS. The compressive deformation by indentation mainly occurs in the PDMS substrate. Therefore, the effect of the PI film on the value of E_{ha} can be ignored. Thus, the relative elastic modulus E^* is approximated as

$$1/E^* \sim (1 - \nu_{hs}^2)/E_{hs} \quad (3)$$

Substituting eq 3 into eqs 1 and 2, we can calculate a and d as a function of the load. Another possible effect of the PI film on the contact state is the increased in-plane tensile modulus, which would result in a slightly smaller indentation (a and d) than the present case neglecting the effect. However, we neglect this effect because here we only focus on the semiquantitative discussion, and the experimentally observed area of contact is roughly in the range of the present estimation as discussed below. Moreover, limitation of the use of the simple Hertzian model, $R \gg a$, is violated in the case of interest. Thus, we also calculated a and d, adopting a Hertz contact theory extended to cover the large indentation[60] (which, however, little affects the semiquantitative discussion below).

When the normal load is low [P = 29.4 mN; e.g., Figures 3b(vii–ix) and 5], $2a$ = 471 μm and d = 55 μm (and those obtained by the extended Hertzian model are $2a$ = 424 μm and d = 46 μm). Because the estimated contact diameter is comparable to the wavelength of the wrinkles (λ = 556 μm at s = 7.5%), two contact states are expected to be realized in which the indenter is supported by two crests or one. For the high-aspect-ratio wrinkles (h = 103 μm), d is approximately half of h. Thus, it is also expected that the center of the indenter cannot make contact with the bottom of the groove throughout the oscillation period. These crude predictions from Hertz contact theory agree well with the present experimental results (Figure 5b–e). For the low-aspect-ratio wrinkles (h = 67 μm at s = 3.5%), $d \sim h$, suggesting that the center of the indenter is expected to be in continuous contact with the surface. This also agrees with the result shown in Figure 7. When the normal load is high [P = 294 mN; e.g., Figures 3b(i–iii) and 6], $2a$ = 1015 μm and d = 257 μm (and those obtained by the extended Hertzian model are $2a$ = 896 μm and d = 214 μm). We can predict that the indenter is supported by the surface extending over two or three crests because $2a \sim 2\lambda$. Moreover, d is larger than h at any strain, suggesting that the center of the indenter squashes the wrinkles and makes continuous contact with the surface. This also agrees with the experimental results (e.g., Figure 6). To summarize this section, the different contact states on wrinkles observed experimentally are qualitatively predicted by Hertz contact theory.

Deformation Cycle Associated with Friction Force Oscillation. Here, we summarize the cycle of deformation of the wrinkles on the basis of the experimental observations (the microscopic images and oscillation in the friction force) and the contact states estimated by Hertz contact theory. Frictional oscillation observed on wrinkles with a high aspect ratio under a low load (Figure 5) is taken as a characteristic result found in the present frictional system. Under this condition, one or two crests are in contact with the indenter during friction, which is experimentally observed and supported by Hertz contact theory. Figure 9 shows a schematic illustration of the friction profile and the corresponding cycle of surface deformation. When a crest is plowed by the front part of the indenter, the

friction force increases because the sheared crest resists the indenter (states 1−3 in Figure 9; multiple-contact state). At the late stage of elastic plowing, the crest passes under the indenter and relaxes shear (and compressive) deformation, decreasing the friction force (states 4−6; single-contact state).

The deformation cycle shown in Figure 9 is slightly modulated when the normal load is high and/or the aspect ratio of the wrinkles is low, as follows. Because the contact area increases under these conditions, the contribution of the periodic plowing at the crest by the frontmost part of the indenter to the total friction force decreases; the amplitude of the friction force oscillation relative to the averaged friction force ($\sim\sigma_F/F_{av}$) is reduced (Figure 8). This result suggests that oscillation of the friction force is further suppressed when the contact area increases further because of, e.g., the use of an indenter that is larger than the period of the wrinkles. This situation would correspond to that reported by Rand and Crosby,[29] in which oscillation of the friction force with a periodicity identical with that of the wrinkles is not observed. (It is interesting to note that the molecular-scale analogue of this scenario has also been predicted for nanofriction on a soft organic monolayer.[56])

Finally, we briefly mention a possible effect of the present laminated structure (the PI film supported by the soft substrate) on the dynamics of the oscillation of friction discussed above. In the present system, additional buckling of the PI film induced by local indentation and sliding of the indenter may occur. Because this additional change in the interfacial shape should not be involved in the dynamics of friction on the simply structured surface of a soft material, this situation is unique for the present laminated structure. In the cycle of surface deformation shown in Figure 9, this effect may be assisting the indenter to pass a crest (states 4−6) because the simply envisaged deformation induced by the indenter can be relaxed slightly by reconfiguring the buckled waveform around the indenter. That is, the top of the crest part is easily displaced in response to the locally applied strain, which is difficult to occur on the simply structured surface of a soft material. (This property is intrinsically the same as the tunability of the wrinkled surface by the applied strain to the whole sample.[46]) Although we cannot confirm the effect from our present experimental results, this may cause a characteristic frictional property on the surface of laminated soft-layered materials and remains to be explored.

CONCLUSIONS

We studied, for the first time, the friction on shape-tunable wrinkles that deformed elastically during sliding. We investigated the effects on the wearless friction of the aspect ratio of the wrinkles, the applied normal load, and the alignment direction of the wrinkles relative to the sliding direction using a pin-on-plate tester at low constant sliding speeds. The size of the rigid hemispherical indenter was comparable to the wavelength of the wrinkles. The friction force oscillated when the sliding direction was perpendicular to that of the wrinkles. The positional relationship between the indenter and wrinkles was clarified by analyzing the spatiotemporal pattern and friction profile. The contact state during the friction was estimated on the basis of Hertz contact theory. As a result, correlation of the friction force oscillation with deformation of the wrinkles was elucidated. In particular, when the crest was elastically plowed by the front part of the indenter, the friction force increased accordingly. When the normal load was high and/or the aspect ratio of the wrinkles was low, the indenter continued to squash the wrinkles and remained in contact with them during sliding; thus, the amplitude of the friction force oscillation relative to the averaged friction force decreased. This result suggests that, under such conditions, the original shape of a soft rough surface, e.g., wrinkles, was reflected less in oscillation of the friction force. We believe that the present results will provide a basis for an understanding of the complicated frictional phenomena in soft living systems. In terms of applications of the present system, the friction and oscillation can be controlled by changing the shape of the wrinkles and/or the applied normal load. Although studying the effects of the sliding speed, adhesion, contact area, humidity, and lubricants on the friction and oscillation will be valuable for future applications, this remains as future work. We envision that such studies may open new directions in tribological research, including haptic interface technologies, antislip/lubricated soft systems, and antifouling.

ASSOCIATED CONTENT

Supporting Information

Real-time observation of the surface deformation during sliding friction on a flat surface and wrinkles under low and high normal loads (mpeg movie file) and typical friction profiles of wrinkles (at s = 7.5% and h = 103 μm) aligned parallel to the sliding direction (Figure S1). This material is available free of charge via the Internet at http://pubs.acs.org.

AUTHOR INFORMATION

Corresponding Authors

*E-mail: kosuke.suzuki@aist.go.jp.
*E-mail: ohzono-takuya@aist.go.jp.

Notes

The authors declare no competing financial interest.

ACKNOWLEDGMENTS

This work was supported in part by the Japanese Ministry of Education, Culture, Sports, Science and Technology via a Grant-in-Aid for Scientific Research on Innovative Areas (Grant 24120003).

REFERENCES

(1) Nosonovsky, M.; Bhushan, B. *Friction, Multiscale Dissipative Mechanisms and Hierarchical Surfaces: Superhydrophobicity, and Biomimetics*; Springer: Berlin, 2008.

(2) Autumn, K.; Liang, Y. A.; Hsieh, S. T.; Zesch, W.; Chan, W. P.; Kenny, T. W.; Fearing, R.; Full, R. J. Adhesive Force of a Single Gecko Foot-Hair. *Nature* **2000**, *405*, 681−685.

(3) Federle, W.; Barnes, W. J. P.; Baumgartner, W.; Drechsler, P.; Smith, J. M. Wet but Not Slippery: Boundary Friction in Tree Frog Adhesive Toe Pads. *J. R. Soc., Interface* **2006**, *3*, 689−697.

(4) Kier, W. M.; Smith, A. M. The Structure and Adhesive Mechanism of Octopus Suckers. *Integr. Comp. Biol.* **2002**, *42*, 1146−1153.

(5) Voigt, D.; Schweikart, A.; Fery, A.; Gorb, S. Leaf Beetle Attachment on Wrinkles: Isotropic Friction on Anisotropic Surfaces. *J. Exp. Biol.* **2012**, *215*, 1975−1982.

(6) Prüm, B.; Bohn, H. F.; Seidel, R.; Rubach, S.; Speck, T. Plant Surfaces with Cuticular Folds and Their Replicas: Influence of Microstructuring and Surface Chemistry on the Attachment of a Leaf Beetle. *Acta Biomater.* **2013**, *9*, 6360−6368.

(7) Bohn, H. F.; Federle, W. Insect Aquaplaning: Nepenthes Pitcher Plants Capture Prey with the Peristome, a Fully Wettable Water-

Lubricated Anisotropic Surface. *Proc. Natl. Acad. Sci. U. S. A.* **2004**, *101*, 14138−14143.
(8) Nonomura, Y.; Miura, T.; Miyashita, T.; Asao, Y.; Shirado, H.; Makino, Y.; Maeno, T. How to Identify Water from Thickener Aqueous Solutions by Touch. *J. R. Soc., Interface* **2012**, *9*, 1216−1223.
(9) Adams, M. J.; Johnson, S. A.; Lefèvre, P.; Lévesque, V.; Hayward, V.; André, T.; Thonnard, J.-L. Finger Pad Friction and its Role in Grip and Touch. *J. R. Soc., Interface* **2013**, *10*, 20120467.
(10) Skedung, L.; Arvidsson, M.; Chung, J. Y.; Stafford, C. M.; Berglund, B.; Rutland, M. W. Feeling Small: Exploring the Tactile Perception Limits. *Sci. Rep.* **2013**, *3*, 2617.
(11) Grosch, K. A. The Relation between the Friction and Visco-Elastic Properties of Rubber. *Proc. R. Soc. London, Ser. A* **1963**, *274*, 21−39.
(12) Persson, B. N. J. Theory of Rubber Friction and Contact Mechanics. *J. Chem. Phys.* **2001**, *115*, 3840−3861.
(13) Tominaga, T.; Kurokawa, T.; Furukawa, H.; Osada, Y.; Gong, J. P. Friction of a Soft Hydrogel on Rough Solid Substrates. *Soft Matter* **2008**, *4*, 1645−1652.
(14) Popov, V. L.; Filippov, A. É. Force of Friction between Fractal Rough Surface and Elastomer. *Technol. Phys. Lett.* **2010**, *36*, 525−527.
(15) Kürschner, S.; Popov, V. L. Penetration of Self-Affine Fractal Rough Rigid Bodies into a Model Elastomer Having a Linear Viscous Rheology. *Phys. Rev. E* **2013**, *87*, 042802.
(16) Pohrt, R.; Popov, V. L.; Filippov, A. E. Normal Contact Stiffness of Elastic Solids with Fractal Rough Surfaces for One- and Three-Dimensional Systems. *Phys. Rev. E* **2012**, *86*, 026710.
(17) Popov, V. L.; Voll, L.; Li, Q.; Chai, Y. S.; Popov, M. Contact Stiffness of Randomly Rough Surfaces. *Sci. Rep.* **2013**, *4*, 3750.
(18) Sneddon, I. N. The Relation between Load and Penetration in the Axisymmetric Boussinesq Problem for a Punch of Arbitrary Profile. *Int. J. Eng. Sci. (Oxford, U.K.)* **1965**, *3*, 47−57.
(19) Johnson, K. L.; Kendall, K.; Roberts, D. Surface Energy and the Contact of Elastic Solids. *Proc. R. Soc. London, Ser. A* **1971**, *324*, 301−313.
(20) Johnson, K. L.; Greenwood, J. A.; Higginson, J. G. The Contact of Elastic Regular Wavy Surfaces. *Int. J. Mech. Sci.* **1985**, *27*, 383−396.
(21) Johnson, K. L. Adhesion and Friction between a Smooth Elastic Spherical Asperity and a Plane Surface. *Proc. R. Soc. London, Ser. A* **1997**, *453*, 163−179.
(22) Guduru, P. R. Detachment of a Rigid Solid from an Elastic Wavy Surface: Theory. *J. Mech. Phys. Solids* **2007**, *55*, 445−472.
(23) Waters, J. F.; Lee, S.; Guduru, P. R. Mechanics of Axisymmetric Wavy Surface Adhesion: JKR-DMT Transition Solution. *Int. J. Solids Struct.* **2009**, *46*, 1033−1042.
(24) Lin, P.-C.; Vajpayee, S.; Jagota, A.; Huid, C.-Y.; Yang, S. Mechanically Tunable Dry Adhesive from Wrinkled Elastomers. *Soft Matter* **2008**, *4*, 1830−1835.
(25) Jin, C.; Khare, K.; Vajpayee, S.; Yang, S.; Jagota, A.; Hu, C.-Y. Adhesive Contact between a Rippled Elastic Surface and a Rigid Spherical Indenter: from Partial to Full Contact. *Soft Matter* **2011**, *7*, 10728−10736.
(26) Kundu, S.; Davis, C. S.; Long, T.; Sharma, R.; Crosby, A. J. Adhesion of Nonplanar Wrinkled Surfaces. *J. Polym. Sci., Part B: Polym. Phys.* **2011**, *49*, 179−185.
(27) Geim, A. K.; Dubonos, S. V.; Grigorieva, I. V.; Novoselov, K. S.; Zhukov, A. A.; Shapoval, S. Y. Microfabricated Adhesive Mmicking Gecko Foot-Hair. *Nat. Mater.* **2003**, *2*, 461−463.
(28) Chateauminois, A.; Fretigny, C. Local Friction at a Sliding Interface between an Elastomer and a Rigid Spherical Probe. *Eur. Phys. J. E: Soft Matter Biol. Phys.* **2008**, *27*, 221−227.
(29) Rand, C. J.; Crosby, A. J. Friction of Soft Elastomeric Wrinkled Surfaces. *J. Appl. Phys.* **2009**, *106*, 064913.
(30) Wu-Bavouzet, F.; Cayer-Barrioz, J.; Le Bot, A.; Brochard-Wyart, F.; Buguin, A. Effect of Surface Pattern on the Adhesive Friction of Elastomers. *Phys. Rev. E* **2010**, *82*, 031806.
(31) Wandersman, E.; Candelier, R.; Debrégeas, G.; Prevost, A. Texture-Induced Modulations of Friction Force: The Fingerprint Effect. *Phys. Rev. Lett.* **2011**, *107*, 164301.
(32) Kim, S. J.; Yoon, J.-I.; Moon, M.-W.; Lee, K.-R. Frictional Behavior on Wrinkle Pattern of Diamond-like Carbon Films on Soft Polymer. *Diamond Relat. Mater.* **2012**, *23*, 61−65.
(33) Audry, M. C.; Fretigny, C.; Chateauminois, A.; Teissere, J.; Barthel, E. Slip Dynamics at a Patterned Rubber/Glass Interface During Stick-Slip Motions. *Eur. Phys. J. E: Soft Matter Biol. Phys.* **2012**, *35*, 83−90.
(34) Ramakrishna, S. N.; Espinosa-Marzal, R. M.; Naik, V. V.; Nalam, P. C.; Spencer, N. D. Adhesion and Friction Properties of Polymer Brushes on Rough Surfaces: A Gradient Approach. *Langmuir* **2013**, *29*, 15251−15259.
(35) Waters, J. F.; Guduru, P. R. A Mechanism for Enhanced Static Sliding Resistance Owing to Surface Waviness. *Proc. R. Soc. London, Ser. A* **2011**, *467*, 2209−2223.
(36) Bowden, N.; Brittain, S.; Evans, A. G.; Hutchinson, J. W.; Whitesides, G. M. Spontaneous Formation of Ordered Structures in Thin Films of Metals Supported on an Elastomeric Polymer. *Nature* **1998**, *393*, 146−149.
(37) Bowden, N.; Huck, W. T. S.; Paul, K. E.; Whitesides, G. M. The Controlled Formation of Ordered, Sinusoidal Structures by Plasma Oxidation of an Elastomeric Polymer. *Appl. Phys. Lett.* **1999**, *75*, 2557−2559.
(38) Brau, F.; Vandeparre, H.; Sabbah, A.; Poulard, C.; Boudaoud, A.; Damman, P. Multiple-Length-Scale Elastic Instability Mimics Parametric Resonance of Nonlinear Oscillators. *Nat. Phys.* **2011**, *7*, 56−60.
(39) Yang, S.; Khare, K.; Lin, P.-C. Harnessing Surface Wrinkle Patterns in Soft Matter. *Adv. Funct. Mater.* **2010**, *20*, 2550−2564.
(40) Schallamach, A. How Does Rubber Slide? *Wear* **1971**, *17*, 301−312.
(41) Rand, C. J.; Crosby, A. J. Insight into the Periodicity of Schallamach Waves in Soft Material Friction. *Appl. Phys. Lett.* **2006**, *89*, 261907.
(42) Ohzono, T.; Suzuki, K.; Yamaguchi, T.; Fukuda, N. Tunable Optical Diffuser Based on Deformable Wrinkles. *Adv. Opt. Mater.* **2013**, *1*, 374−380.
(43) Ohzono, T.; Shimomura, M. Ordering of Microwrinkle Patterns by Compressive Strain. *Phys. Rev. B* **2004**, *69*, 132202.
(44) Ohzono, T.; Watanabe, H.; Vendame, R.; Kamaga, T.; Ishihara, T.; Kunitake, T.; Shimomura, M. Spatial Forcing of Self-Organized Microwrinkles by Periodic Nanopatterns. *Adv. Mater.* **2007**, *19*, 3229−3232.
(45) Ohzono, T. Control of Cooperative Switching of Microwrinkle Orientations by Nanopatterns. *Chaos* **2009**, *19*, 033104.
(46) Ohzono, T.; Monobe, H. Microwrinkles: Shape-Tunability and Applications. *J. Colloid Interface Sci.* **2012**, *369*, 1−8.
(47) Ohzono, T.; Monobe, H.; Yamaguchi, R.; Shimizu, Y.; Yokoyama, H. Dynamics of Surface Memory Effect in Liquid Crystal Alignment on Reconfigurable Microwrinkles. *Appl. Phys. Lett.* **2009**, *95*, 014101.
(48) Kim, S.-C.; Israr, A.; Poupyrev, I. Tactile rendering of 3D features on touch surfaces. *Proceedings of the 26th Annual ACM Symposium on User Interface Software and Technology (UIST'13)*, St. Andrews, U.K., October 8−11, 2013; ACM: New York, 2013; pp 531−538.
(49) Wang, C.; Hwang, D.; Yu, Z.; Takei, K.; Park, J.; Chen, T.; Ma, B.; Javey, A. User-Interactive Electronic-Skin for Instantaneous Pressure Visualization. *Nat. Mater.* **2013**, *12*, 899−904.
(50) Gong, J. P.; Iwasaki, Y.; Osada, Y.; Kurihara, K.; Hamai, Y. Friction of Gels. 3. Friction on Solid Surfaces. *J. Phys. Chem. B* **1999**, *103*, 6001−6006.
(51) Adams, M. J.; Briscoe, B. J.; Wee, T. K. The differential friction effect of keratin fibres. *J. Phys. D: Appl. Phys.* **1990**, *23*, 406−414.
(52) Kaneko, D.; Oshikawa, M.; Yamaguchi, T.; Gong, J. P.; Doi, M. Friction Coefficient between Rubber and Solid Substrate—Effect of Rubber Thickness. *J. Phys. Soc. Jpn.* **2007**, *76*, 043601.
(53) Tomlinson, G. A. A Molecular Theory of Friction. *Philos. Mag.* **1929**, *7* (1798−1977), 905−939.

(54) McClelland, G. M.; Glosli, J. N. In *Fundamental of Friction: Macroscopic and Microscopic Processes*; Singer, I. L., Pollock, H. M., Eds.; Kluwer: Dordrecht, The Netherlands, 1992; pp 405−425.
(55) Sokoloff, B. J. Fundamental Mechanisms for Energy Dissipation at Small Solid Sliding Surfaces. *Wear* **1993**, *167*, 59−68.
(56) Ohzono, T.; Fujihira, M. Molecular Dynamics Simulations of Friction between an Ordered Organic Monolayer and a Rigid Slider with an Atomic-Scale Protuberance. *Phys. Rev. B* **2000**, *62*, 17055−17071.
(57) Ying, Z. C.; Hsu, S. M. First Observation of Elastic Plowing in Nanofriction. *Proceedings of World Tribology Congress III (WTC2005)*, Washington, DC, Sept 12−16, 2005; ASME: New York, 2005; pp 339−340.
(58) Hertz, H. In *Miscellaneous Papers*; Jones, D. E., Schott, G. A., Eds.; Macmillan: London, 1896; pp 146−162.
(59) Popov, V. I. *Contact Mechanics and Friction*; Springer: Berlin, 2010.
(60) Liu, D. X.; Zhang, Z. D.; Sun, L. Z. Nonlinear elastic load−displacement relation for spherical indentation on rubberlike materials. *J. Mater. Res.* **2010**, *25*, 2197−2202 . Note that the contact area *a* and the penetration depth *d* regarding the extended Hertz contact theory reported in this reference were calculated using eqs 4 and 5 in their report, which agree well with the relevant experiments. We numerically solved the problem because *a* is the solution of the fifth-order equation.